Prediction of Diffusive Transport Through Polymer Films From Characteristics of the Pore Geometry

Sandra Barman, Holger Rootzén and David Bolin
Dept. of Mathematical Sciences, Chalmers University of Technology and the University of Gothenburg, Gothenburg, Sweden

DOI 10.1002/aic.16391
Published online in Wiley Online Library (wileyonlinelibrary.com)

Diffusive transport through porous materials is to a large extent determined by the microstructure of the material. To design materials with controlled transport properties, it is hence important to connect properties of the pore geometry to diffusive transport rates. Different kinds of microstructures from a stochastic model are generated and multiplicative regression is used to find relationships between geometric measures of the microstructures and numerically simulated diffusive transport. The main results are that the geodesic tortuosity explains a large part of the transport variation, and that the standard deviations we introduce further improves prediction. It was found that it is best to compute the tortuosity using the whole pore space, instead of using only the inlet, as is commonly done. The effects of calculating the measures using small samples of the pore structure were investigated, and a method for minimizing errors resulting from boundary effects was proposed. © 2018 American Institute of Chemical Engineers *AIChE J*, 00: 000–000, 2018

Keywords: diffusive transport, porous media, pore geometry characterization, transport prediction, boundary effects

Introduction

With microscopes becoming more and more powerful, the three-dimensional microstructure of porous materials can now be imaged in great detail.[1-3] Advances in computational power over the last decades have made possible numerical simulation of mass transport in the complicated geometric structures obtained from the microscopy images.[4,5] Connecting the microstructure in the images to transport properties is important in fields as diverse as composite materials design,[6] electrochemical engineering,[7] the oil and gas industry,[8] and biomedical and pharmaceutical science.[9-11] Our work concerns porous polymer films which are used as coatings to control the rate of drug release from pharmaceutical pellets. The pore structure, and thus its diffusive mass transport, can be altered by changing the processing parameters and the polymer composition.[12,13] To aid the design of coatings with tightly controlled transport properties it is important to be able to connect the pore geometry to the transport properties. In this article we propose a new measure of transport, the transport ratio, which helps understanding of how geometric properties influence diffusive transport, and new geometric measures which predict the transport ratio better than previously used ones. We also quantify boundary effects caused by the necessity of using a finite sample from the film for numerical simulation of mass transport and for computation of geometric measures, and propose an approach to reduce errors caused by boundary effects.

These results are based on the analysis of random samples of pore structures simulated from a stochastic model. Simulation has the advantage that new structures can easily be generated from the model, whereas preparing the polymer films and performing the microscopy is a time-consuming and costly process which poses difficult questions of homogeneity and reproducibility. Additionally a stochastic model can easily be changed to generate different kinds of pore structures, whereas tailoring the production process to generate polymer films with desired properties can be difficult. Here we use a three-dimensional thresholded stochastic Gaussian field model for the pore structure of the porous polymer films. The parameters for our model were obtained by fitting it to confocal laser scanning microscopy images of polymer films, see Barman and Bolin.[14] The samples generated from the model are considered to be samples from an ergodic stochastic film which is infinite in the x,y-direction, but finite (and "thin") in the z-direction, which is the direction of mass transport.

Gaussian random field based models were among the first stochastic models used to reconstruct heterogeneous materials[15] (p. 295), and were in, for example, Adler et al.,[16] Roberts and Teubner,[17] Mukherjee and Wang[18] used to connect macroscopic properties to the microstructure of porous media. Our new model was found to fit the type of porous polymer film we study well.[14] Gaussian field models, however, are only suitable for some types of porous media.[19] Our model was found to fit the type of porous polymer film we study well.[14] A larger range of pore geometries, for example, for particle based systems, can be obtained using simulated annealing based reconstructions[20] and pattern-based simulation methods.[21,22] Examples of other types of stochastic models that have been used to connect microstructure to transport properties can be found in Blunt et al.,[8] Kim and Pitsch,[23] and Stenzel et al.[24]

Additional Supporting Information may be found in the online version of this article.

Correspondence concerning this article should be addressed to S. Barman at barmane@chalmers.se

There are several characterization measures that have been used to correlate properties of the pore geometry with the diffusive transport. In particular, pore volume and tortuosity have a long history of being used to predict diffusive transport, see the review in Ghanbarian et al.[25] Here tortuosity attempts to measure the "windedness" of the pores. There is no consensus about how to best define a measure of tortuosity. We argue for using one definition of the geodesic tortuosity over more common definitions, and compare the predictive power of the definitions. We also include the standard deviation of the geodesic tortuosity, which in addition to measuring the variation of path lengths from inlet to outlet is also a measure of the prevalence of dead-end pores.

Pore size variation also influences transport ratios and, in particular, bottlenecks can reduce the transport rate greatly.[26] A measure to capture bottleneck effects, "constrictivity," was recently introduced in Holzer et al.,[27] and shown to be useful for predicting diffusive transport rates in Stenzel et al.[24] We propose to use the standard deviation of the pore size as an alternative to constrictivity, which also in a sense captures bottleneck effects, but has better predictive properties for our dataset.

Following the literature, we fit multiplicative models to predict transport ratios from the geometric measures. We use stepwise regression to remove predictors that are not statistically significant from the models in a systematic way. This makes it possible to compare the importance of new and old predictors.

The next section gives a short overview of transport prediction models, introduces new prediction tools, and applies them to the simulated samples. The following section studies the effects of limited sample window sizes, and the last section summarizes our main conclusions.

Background on Transport Prediction

Transport is guided by the diffusion equation

$$\mathbf{J} = -D_0 \nabla c, \tag{1}$$

along with mass conservation

$$\frac{\partial c}{\partial t} = \nabla \cdot \mathbf{J}, \tag{2}$$

where c is concentration, D_0 is the diffusion coefficient, and $\mathbf{J} = (J_x, J_y, J_z)$ is the diffusive flux. For a porous film, diffusion is driven by a difference between the concentration $c = c_{\text{in}}$ at the inlet $z = 0$ and the concentration $c = c_{\text{out}}$ at the outlet $z = L_z$.

The transport properties of a pore structure are commonly characterized by the effective diffusion coefficient D_{eff} defined analogously to Eq. 1 as

$$\langle J_z \rangle = -D_{\text{eff}} \widetilde{\nabla} c, \tag{3}$$

where $\langle J_z \rangle$ is the diffusive flux in the z-direction averaged over the whole structure and $\widetilde{\nabla} c = (c_{\text{out}} - c_{\text{in}})/L_z$. Due to the linearity of Eq. 1, D_{eff} is invariant under changes in $\widetilde{\nabla} c$.

Important geometric factors that can be used to predict D_{eff} are the volume fraction of connected pores, the tortuosity, pore connectivity, and variations in pore size[10] (Ch. 9).

Porosity

There have been many attempts to predict the mean transport rate from the pore geometry. The simplest one is Archie's law,[28]

$$\frac{D_{\text{eff}}}{D_0} = \epsilon^m, \tag{4}$$

where ϵ is the pore volume fraction, or porosity. Here the exponent m is obtained from fitting Eq. 4 to experimental data, for ϵ far above the percolation threshold. Many other methods for using the pore fraction as predictor have been developed, see Ref. 25.

Tortuosity

A development of Archie's formula that has been extensively used is

$$\frac{D_{\text{eff}}}{D_0} = \frac{\epsilon}{\tau^k}, \tag{5}$$

where τ is called the tortuosity factor, or just the tortuosity, and $k = 1$ or $k = 2$ are the most commonly used values for its exponent. The tortuosity is intended to account for the effect of increased pore lengths due to winding pore paths. There is a substantial literature on tortuosity, see the reviews of Ghanbarian et al.[25] and Shen and Chen.[29]

When experimental data on D_{eff} and D_0 were available but there were no data on pore geometry the tortuosity was simply defined through Eq. 5, as $\tau = (\epsilon D_0/D_{\text{eff}})^{1/k}$. This definition of τ, sometimes termed the diffusive tortuosity, is still widely used[25] (p. 1464). However, τ then includes all factors that lessen the transport rate apart from the volume fraction, and not just the winding of pores the tortuosity is supposed to account for. This is a common criticism of Eq. 5.

It has been claimed that the purpose of setting $k = 2$ in Eq. 5 has been to obtain tortuosities of reasonable magnitude.[26,27] However, the square has been derived theoretically in the context of diffusion[30] and in the context of flow[31] (pp. 12–13). See Epstein[32] for an overview of the confusion regarding whether the tortuosity should be squared or not.

Advances in 3D microscopy have enabled direct calculations of tortuosity from the geometric structure of the pores. The starting point is the pointwise geodesic tortuosity which is defined as $\tau(p) = L(p)/L_z$, where $L(p)$ is the length of the shortest path through the pore space which goes from the inlet to the outlet passing through the point p, and L_z is the width of the film. Several different methods for computing a geodesic tortuosity factor τ from the pointwise tortuosities can be constructed. A common one, used in Stenzel et al.[24] and Pecho et al.,[33] is

$$\tau_{\text{inlet}} = \frac{1}{|P_{\text{In}}|} \int_{p \in P_{\text{In}}} \tau(p) dp, \tag{6}$$

where P_{In} denotes the pores at the inlet. A related tortuosity factor is the geometric tortuosity, which is instead calculated on a skeleton extracted from the pore space.[34,35] It is common also here to calculate the geometric tortuosity using only pointwise tortuosities at the inlet. In Stenzel et al.,[24] the geodesic tortuosity was found to outperform the geometric tortuosity in terms of predicting diffusive transport.

Constrictivity

Unreasonably high tortuosity values were sometimes obtained when Eq. 5 was used as the definition of tortuosity.[26] To remedy this, in Owen[36] and Petersen,[26] additional properties of the pore geometry were incorporated into Eq. 5 to give the formula

$$\frac{D_{\text{eff}}}{D_0} = \frac{\epsilon\beta}{\tau^k}. \tag{7}$$

Here β is a constrictivity factor which accounts for variations in pore width.

The original definition of constrictivity for a straight pore with varying widths was $\beta = A_{\min}/A_{\max}$, where $A_{\max}$ and $A_{\min}$ are the largest and smallest cross-sectional areas, respectively. Alternative definitions of the constrictivity factor have been suggested for more complex pore geometries in Berg[37] and Holzer et al.[27] In the latter reference the median pore size is used to define $A_{\max}$ and the median of the related mercury intrusion porosimetry-pore size (MIP-pore size) to define $A_{\min}$. The MIP-pore size of a point is the size of the largest sphere that can travel through the pore space from the inlet to the point. It provides a measure of bottleneck sizes. It has been proved useful also in other contexts as a measure of interconnectivity, see Camp et al.[38] and Moore.[39] Replacing Eq. 5 with Eq. 7 using this constrictivity factor was in Stenzel et al.[24] found to substantially reduce the error in predicting D_{eff}. More generally, several equations of the form $\frac{D_{\text{eff}}}{D_0} = \frac{a\epsilon^m\beta^l}{\tau^k}$, with coefficients a, m, l, and k fitted to data, were in this paper evaluated with respect to their transport prediction properties.

New Tools

Our aim is to contribute to the understanding how the geometry of the pore structure influence transport and in particular efficient prediction of transport from quantitative geometric predictors. We consider the following predictors: the volume fraction; the volume fraction of connected pores; the mean pore size; the mean MIP-pore size; the constrictivity measure that was found to have the greatest predictive capability in Stenzel et al.,[24] as described in the previous section; a new variant of the geodesic tortuosity; and the standard deviations of pore size, the MIP-pore size, and the geodesic tortuosity. The pointwise values of the tortuosity, the pore size, and the MIP-pore size, illustrated in Figure 1, are thus used to calculate all predictors except the volume fractions. The use of standard deviations for prediction is new. We have found the concept of transport ratio, as defined below, useful both for understanding and for prediction.

Transport ratio

The transport ratio TR is defined by

$$\text{TR} = \frac{D_{\text{eff}}}{D_0\epsilon}. \tag{8}$$

By Eq. 3 we have that $\text{TR} = \langle J_z\rangle / \left(-\epsilon D_0 \widetilde{\nabla} c\right)$, and hence the transport ratio is the ratio of the mean transport rate $\langle J_z\rangle$ of the pore structure, to the mean transport rate $-\epsilon D_0 \widetilde{\nabla} c$ of a pore structure with the same volume fraction ϵ but with straight pores aligned with the direction of transport. The Wiener bounds, first proved in Wiener,[40] imply that for a porous ergodic film $\text{TR} \le 1$.[15] The bound is attained for a pore structure with straight pores, which hence has the most efficient, or "optimal," transport for the given volume fraction. Thus the transport ratio relates the transport rate of the film to the transport rate of the optimal pore structure.

The transport ratio is related to the diffusive tortuosity defined by Eq. 5 as $\text{TR} = 1/\tau^k$. The interpretability of the diffusive tortuosity discussed above is solved by the transport ratio. The transport ratio has been used in the gas diffusion literature, where it is termed pore continuity[25] (p. 1464), though as far as we can tell without the interpretation we provide above.

Average of the reciprocal of the pointwise geodesic tortuosity

We propose the definition of the tortuosity to be $1/\tau^2 = \langle 1/\tau(p)^2\rangle$ for an infinite ergodic film, with the average taken over the pore space, and thus that for a sample of the film τ is computed as

$$\frac{1}{\tau^2} = \frac{1}{|P|}\int_{p\in P} \frac{1}{\tau(p)^2} dp, \tag{9}$$

where P is the pore space of the sample. A similar expression was used in the context of hydraulic flow in Dullien,[41] Section 4.9.2.1. We choose this definition partly because then, as argued next, $\text{TR} = 1/\tau^2$ for straight pores with constant cross-section, and partly because $1/\tau^2$ defined in this way has an intuitive interpretation in terms of the transport ratio for more complex pore structures.

To see that $\text{TR} = 1/\tau^2$ for straight pores with constant cross-section we assume that the sample has pores $p_1, \ldots, p_n$ with volume V_k, $k = 1, \ldots, n$ and that the pointwise geodesic tortuosity is constant in each pore, and denote it by τ_k. Recall that this means that the length of pore k is τ_k times the width of the film. Then the integral in Eq. 9 simplifies to $1/\tau^2 = \frac{\sum_k V_k/\tau_k^2}{\sum_k V_k}$. We further make the simplifying assumption that the concentration derivative in the direction of the pore's path is constant. The directional concentration derivative is then reduced by a factor $1/\tau_k$ compared to a straight pore going in the z-direction, due to the increased length of the pore, and hence the

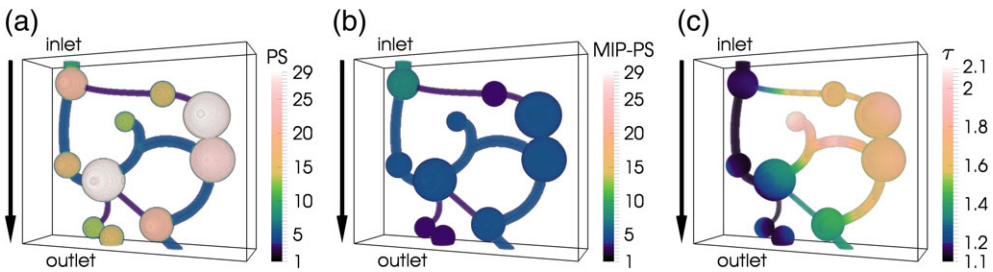

Figure 1. Pointwise measures, (a) pore size, PS, (b) MIP-pore size, MIP-PS, and (c) tortuosity, τ, computed in an idealized pore structure. The pore size and MIP-pore size are given as the fitted spheres' radii in number of voxels, and are shown with the same color-scale. The black arrow indicates the direction of transport.
[Color figure can be viewed at wileyonlinelibrary.com]

directional flux in the z-direction is $-D_0\widetilde{\nabla}c/\tau_k$. Since the pore has constant cross-section, the cross-sectional area equals $V_k/(\tau_k L_z)$. The cross-section is perpendicular to the pore's path, which means that the transport through the pore is the area of the cross-section times the directional flux, which is $-V_k/(\tau_k L_z)D_0\widetilde{\nabla}c/\tau_k$. We can compare this to the transport through a pore in the z-direction with the same volume V_k, which would be $-V_k/L_z D_0\widetilde{\nabla}c$. The transport is thus reduced by a factor $1/\tau_k^2$, where one factor $1/\tau_k$ comes from the reduction of the concentration derivative, and one factor $1/\tau_k$ comes from the reduction of the cross-sectional area, compared to the straight pore going in the z-direction. The transport through the whole pore system is $-D_0\widetilde{\nabla}c\sum_k V_k/\left(L_z\tau_k^2\right)$. It follows that the transport ratio can be written as

$$\mathrm{TR}=\frac{-D_0\widetilde{\nabla}c\sum_k V_k/\left(L_z\tau_k^2\right)}{-D_0\widetilde{\nabla}c\sum_k V_k/L_z}=\frac{\sum_k V_k/\tau_k^2}{\sum_k V_k},$$

and hence, assuming the simplifying assumptions, $\mathrm{TR} = 1/\tau^2$.

Thus the geodesic tortuosity factor τ determines the total diffusive transport through straight pores with constant cross-section. It follows that the ratio between the transport ratio through a complex pore structure and $1/\tau^2$ indicates how much the transport ratio depends on the tortuosity and how much it is influenced by other factors. This since $1/\tau^2$ is the transport ratio of a pore structure with straight pores and the same pointwise tortuosities as the complex pore structure.

The difference between τ and τ_{inlet} as defined by Eq. 6 can be substantial, and so $1/\tau_{\mathrm{inlet}}^2$ can not be interpreted in terms of the contribution of the tortuosity to the transport ratio. A major difference is that τ takes the average over the whole pore space rather than just over the inlet, and hence incorporates more information about the pore geometry than τ_{inlet}. This is illustrated in Figure 1c, where the difference between the pointwise tortuosity at the inlet and outlet is markedly different from the average over the whole pore space. These points, and the importance of using the average over the inverse of the point-wise tortuosities squared as in Eq. 9, are further illustrated in the Supporting Information.

Standard deviation

To the extent of our knowledge, standard deviations have not been used before to predict transport thorough pore structures. We include the standard deviations of the pointwise tortuosity, pore size, and MIP-pore size as predictors.

Stochastic Simulation Experiment

We use the following stochastic simulation experiment to find predictors of transport and to investigate how to handle boundary effects.

Model

The parametric family of stochastic models developed in Barman and Bolin[14] was used to generate samples of pore structures. The family is aimed at modeling pore structures in ethylcellulose/hydroxypropylcellulose (EC/HPC) films from Häbel et al.[42] Using estimated covariance functions; a number of geometric goodness of fit measures; and comparing numerically simulated diffusion in the films with diffusion in simulated samples from the model, this family was in Barman and Bolin[14] shown to give good fit to 3D confocal laser scanning microscopy (CLSM) images of two EC/HPC free films, one with 30% HPC and the other with 40% HPC.

In the models pore structures were obtained by thresholding and smoothing stochastic simulations of a Gaussian random field. For each simulation the threshold was set so that the simulated pore structure had the desired volume fraction. The distribution of a Gaussian field is determined by its mean and covariance function.[43] In our models, the mean function is zero, and the covariance functions are members of a family of separable oscillating Matérn covariance functions of the form $C(x, y, z) = C_z(z)C_{x,y}(\|x - y\|)$, with $C_z(z)$ a one-dimensional oscillating Matérn covariance function and $C_{x,y}(\|x - y\|)$ a two-dimensional isotropic oscillating Matérn covariance function.[44] The separability of the covariance function C allows for different behavior along the depth of the pore structures (the z-direction), and in planar sections (the x,y-plane). Separating the control of the depth and planar section of the model in this way was motivated by the shapes of the pores in the CLSM images of the EC/HPC films.

The shape of the covariance functions C_z and $C_{x,y}$, in the z-direction and in the x,y-plane are controlled by regularity parameters θ_z and $\theta_{x,y}$, respectively, see Figure 2. The distances from the origin to the first peak of the covariance functions are the same for all models in this article, and can be interpreted as a typical distance between peaks of the Gaussian field along the depth and in the planar sections, respectively. Stronger oscillations of the covariance function, that is, higher values of θ_z and/or $\theta_{x,y}$, lead to stochastic simulations where these typical distances are more closely adhered to, and thus more regular pore structures, see Figure 3.

Additionally, lower θ_z-values leads to pores which are more elongated in the z-direction, that is, pores which are less winded. More information about the model can be found in Barman and Bolin.[14]

Setup

The main stochastic simulation experiment was aimed at prediction of transport. We considered $4 \times 3 \times 3 = 36$ stochastic pore structure models. These models were obtained using four pore volume fractions $\epsilon = 0.25, 0.3, 0.4, 0.5$, and three values of each of the regularity parameters $\theta_{x,y}$ and θ_z, which were set to either a low, a medium, or a high value, see Figures 3 and 4. The exact values were $\theta_{x,y} = 0.5, 0.8, 0.95$, and $\theta_z = 0.4, 0.7, 0.95$. These values were chosen to obtain a wide range of pore geometries. For the combination where both $\theta_{x,y}$ and θ_z were set to a high value, we used $\theta_{x,y} = 0.95$ and $\theta_z = 0.9$ due to high computational cost of calculating the diffusion with $\theta_z = 0.95$.

We simulated six samples of pore structures of size $250 \times 250 \times 250$ from each of the 12 models. The limiting factor for the size of the samples was the computational cost for the numerical calculation of diffusion through the pore structures. To avoid boundary effects we computed the geometric predictors and the diffusion in the entire sample, but only used central subsamples of size $226 \times 226 \times 250$ for prediction, see the section "Effects of limited sample window size."

In a second experiment we used $\epsilon = 0.3$, a high $\theta_{x,y}$ and low θ_z, and simulated 36 pore structures of various sizes from this model. These were used to compare the methods (9) and (6) to compute tortuosity, and to evaluate boundary effects.

Computation

In order to use 9 the pointwise geodesic tortuosities $\tau(p)$ has to be computed for all points in the pore space. We used Matlab's function bwdistgeodesic,[45] which returns the

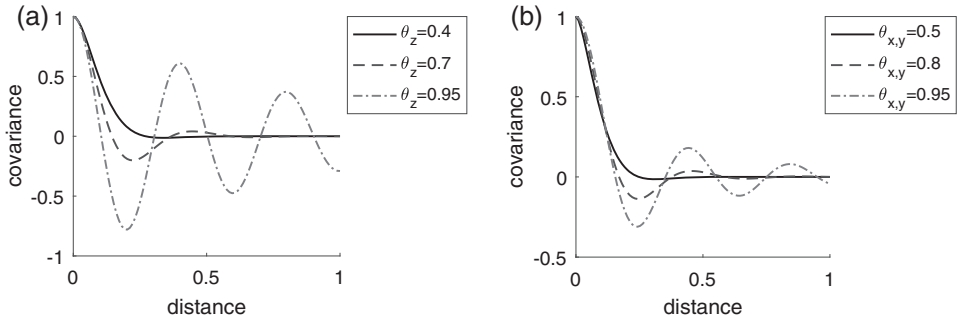

Figure 2. Covariance functions (a) C_z and (b) $C_{x,y}$, for different values of the regularity parameters θ_z and $\theta_{x,y}$.

geodesic distance from all points in the pore space to a set of seed locations, to develop the following algorithm: choose as seed locations the inlet and the outlet, respectively. This gives the geodesic distance from all points to both the inlet and the outlet. The distance of the shortest path through the pore space which goes from the inlet to the outlet and which passes through a point is obtained by summing the distance to the inlet and the distance to the outlet. Dividing by the width L_z of the sample then gives the pointwise tortuosity, which we obtain for all points in the pore space.

To compute τ_{inlet} instead, only the outlet is chosen as seed locations, which amount to about half the calculations performed to find the pointwise tortuosity for all points. Thus by doubling the number of calculations, we get the pointwise tortuosity for all the points in the pore space, instead of just for the points at the inlet.

Computation of pore size and MIP-pore size were done using the Matlab functions bwdist, imdilate, and imfill.[45] Descriptions of how to implement the pore size measures are given in Münch and Holzer.[46]

We calculate diffusion numerically in the pore structures with the software Gesualdo.[47] Gesualdo uses the lattice-Boltzmann method. The diffusion Eqs. 1 and 2 are solved in the pore space until steady state, that is, until $\frac{\partial c}{\partial t} = 0$. No-flux boundary conditions $\mathbf{J} \cdot \mathbf{n} = 0$ are applied at the pore interfaces, where $\mathbf{n}$ is a vector normal to the interface.[48] The diffusive transport is driven by a concentration gradient along the depth of the sample window (the z-direction), that is we set $c = c_{\text{in}}$ at the inlet ($z = 0$) and $c = c_{\text{out}}$ at the outlet ($z = L_z$). Mirror boundary conditions are applied at the other boundaries of the sample window.

To fit the regression models used to predict the transport ratio, we used Matlab's stepwiselm for the stepwise linear regression, and nlinfit for the nonlinear regression.[45] Programs were implemented in Matlab and computations performed on resources at Chalmers Centre for Computational Science and Engineering provided by the Swedish National Infrastructure for Computing.

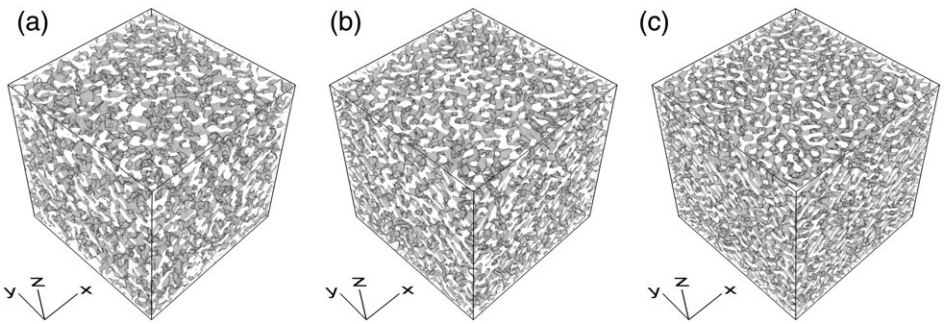

Figure 3. Pore structures obtained with ϵ = 30% and different values of the regularity parameters $\theta_{x,y}$ and θ_z: (a) low values, (b) medium values, and (c) high values.

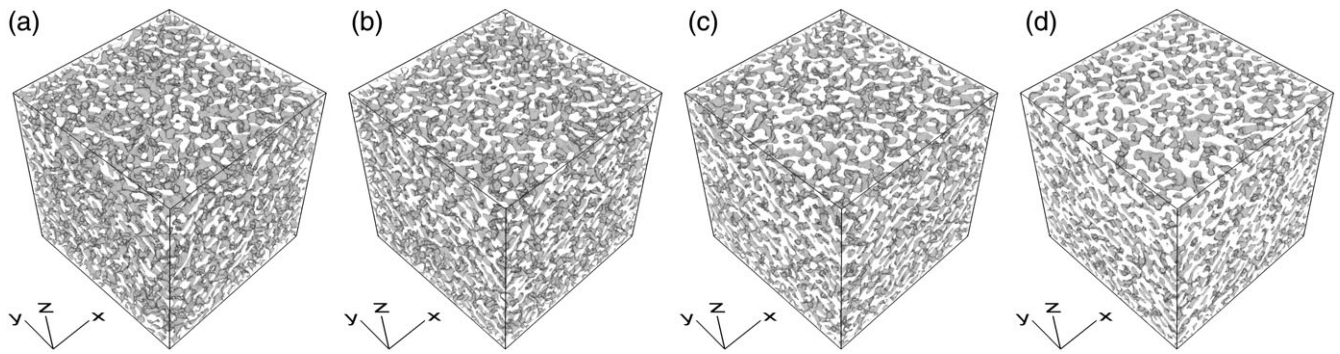

Figure 4. Pore structures obtained with medium regularity parameter values and different pore volume fractions: (a) ϵ = 20%, (b) ϵ = 30%, (c) ϵ = 40%, and (d) ϵ = 50%.

Prediction of Transport Ratio

Transport ratios

The transport ratios vary within a large range, from 0.09 to 0.80. The mean transport ratio increases from 0.2 for $\epsilon = 0.25$ to 0.6 for $\epsilon = 0.5$, and for each volume fraction the transport ratio is highest for the model with a high $\theta_{x,y}$-parameter and a low θ_z-parameter, and lowest for the reversed parameter combination, see Figure 5. Recall that decreasing the $\theta_{x,y}$ and θ_z parameters results in pore structures with higher disorder.

Even though transport ratios show a similar pattern for each volume fraction, flux behaves quite differently for different volume fractions, see Figure 6. In this figure, flux J_z was normalized by the magnitude $|\mathbf{J}_{\text{opt}}| = |J_{z,\text{opt}}| = |D_0 \widetilde{\nabla} c|$ of the flux $\mathbf{J}_{\text{opt}}$ in an optimal pore structure, analogously to the way the mean flux was normalized to obtain the transport ratio. This means that the transport ratio can be expressed as the average of the normalized flux, that is, as $\text{TR} = \frac{1}{|P|}\int_{p\in P} J_z/|\mathbf{J}_{\text{opt}}|\,dp$, where P is the pore space. The histograms for models with lower volume fractions have a heavier right tail, indicating the influence of bottlenecks where flux tends to be high. Lower volume fraction histograms also have a higher portion of flux that is close to zero, and thus a greater portion of the pore space that does not contribute to the diffusive transport.

Prediction

We performed stepwise linear regressions of the logarithm of the transport ratio using the logarithm of the geometric measures listed in Table 1 as predictors (detailed results for the predictors can be found in the Supporting Information). The regression results are listed in Table 2. The stepwise regression removes predictors based on their statistical significance, and does not include predictors that are linearly dependent. We only included regression models that were stable. By a stable model, we mean a model that is not sensitive to removing some of the data-points. That is the fitted model coefficients may change slightly, but the predictors chosen by the stepwise regression essentially remains the same when a randomly chosen third of the observations are excluded from the dataset. The model where all predictors were included was very unstable, and as a consequence was not used.

The best model from Table 2, with the highest R^2 value, $\text{TR} \sim \frac{a}{\tau^b \sigma_\tau^c}$, was quite stable. To investigate other interesting models, we excluded some subsets of the predictors. The second best model, $\text{TR} \sim \frac{a\epsilon_c^b \text{PS}^c}{\tau^d \sigma_{\text{PS}}^e}$, was less stable, but still the tortuosity, PS and σ_{PS} were chosen quite consistently. The third model included in the table, $\text{TR} \sim \frac{a\beta^b}{\tau^c}$, was not the third best fit, but was included for comparison since this model was used in Stenzel et al.[24] The fit was not stable, as only τ was included in more than half of the fits when a random third was excluded from the dataset. The fit is similar to the model $\text{TR} \sim \beta^a/\tau^b$ fitted in Stenzel et al.,[24] where the fitted values were $a = 0.36$ and $b = 5.17$. Regression models that include ϵ, β, and τ were also used in Stenzel et al.[24] For our dataset however, β was not significant when ϵ was also allowed as a predictor, and this combination is therefore not included in the table. The fourth model, $\text{TR} \sim \frac{a}{\tau^b}$, was very stable. All fitted models perform very well in predicting the transport ratio, as indicated by the root mean squared errors (MSEs) and the explained variation (the R^2 values).

The residuals of the logarithmic regression are the logarithms of the quotient between the fitted values of the corresponding multiplicative model and TR and hence correspond to residuals of different sizes in the multiplicative model. To assess the effect of this we also fitted the multiplicative model directly, that is, we fit the multiplicative model obtained from the logarithmic linear regression, but determine the coefficients using nonlinear regression. Table 2 shows that, as expected, errors were smaller for the direct multiplicative than for the logarithmic regression, but differences were small. The ordering of the models was preserved, with the best model being $\text{TR} \sim \frac{a}{\tau^b \sigma_\tau^c}$ in both cases.

The plots in Figure 7 show a good fit of the model $\text{TR} \sim \frac{a}{\tau^b \sigma_\tau^c}$. The corresponding plots for the other models were similar.

Above it was argued that $1/\tau^2$ is the transport ratio of a pore structure where tortuosity is the only factor which lowers the transport rate. Hence we also fitted the models in Table 2 with the exponent of the tortuosity factor fixed as $1/\tau^2$. Table 3 shows that the models that include the standard deviations σ_τ and σ_{PS} then still explain a large part of the variation in the transport rate. The model which used the constrictivity β on the other hand performed much worse. The ordering of models was the same as before.

Comparison of Methods to Compute the Geodesic Tortuosity. For our dataset, the difference between τ and τ_{inlet}, as given by Eqs. 9 and 6 was between 0.3% and 15%. The differences were mainly caused by taking the mean of $\tau(p)$ over the whole pore space instead of only at the inlet. The tortuosity factor τ was consistently chosen by the stepwise regression and not τ_{inlet}. If τ was excluded from the predictors and τ_{inlet} was used instead, the fit was worse, but still the difference was small.

For further comparison we used the second simulation experiment. This only included a single model ($\epsilon = 0.3$, high $\theta_{x,y}$ and low θ_z) so that differences between the simulated samples only were due to random variation and therefore involved a much smaller range of computed transport ratios. The model $\text{TR} \sim a/\tau_{\text{inlet}}^b$ then gave an R^2 value 0.05, and did not even lead to a significant improvement compared to the constant model. The model $\text{TR} \sim a/\tau^b$ on the other hand explained a

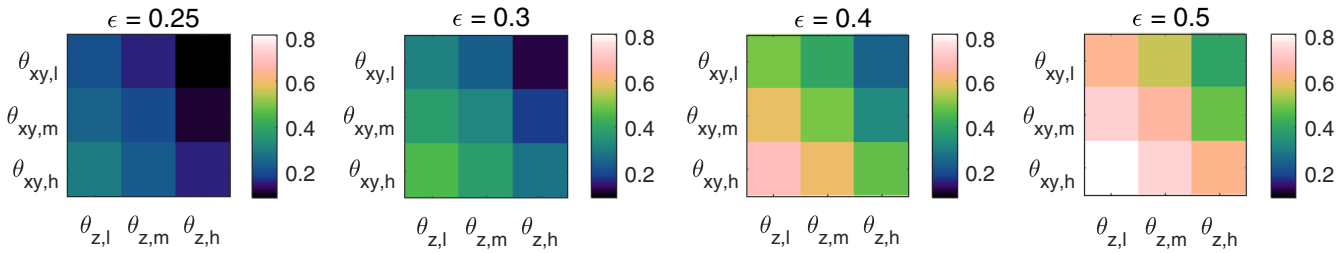

Figure 5. The transport ratio TR for all stochastic models.

The squares are grouped by pore volume fraction ϵ, and each square represents one model. $\theta_{\star,l}$, $\theta_{\star,m}$, $\theta_{\star,h}$ are the low, medium, and high regularity parameters, respectively. [Color figure can be viewed at wileyonlinelibrary.com]

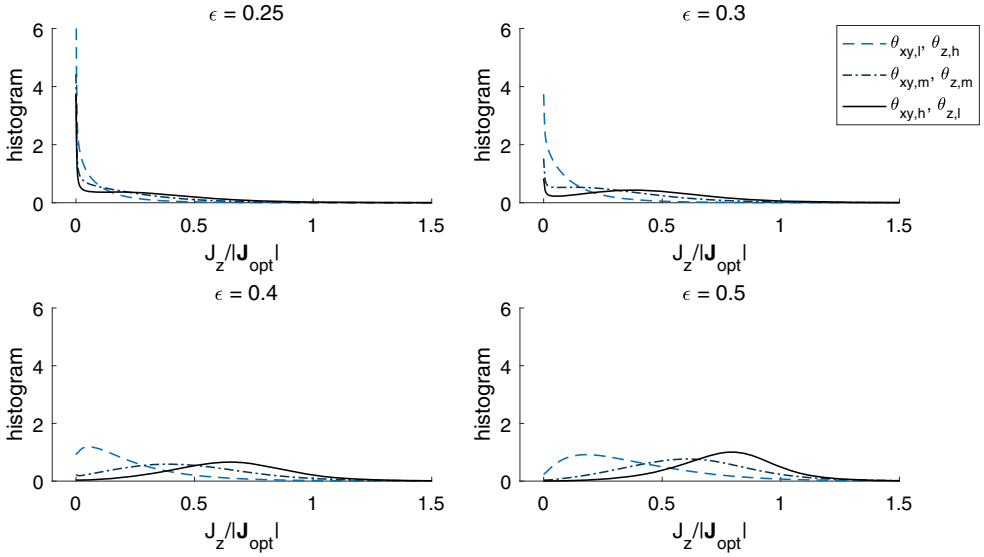

Figure 6. Mean histograms of the normalized flux, shown as continuous functions, for three of the stochastic models for each volume fraction.

The histograms were normalized to sum to one, and the *y* axis was cut off at six. [Color figure can be viewed at wileyonlinelibrary.com]

Table 1. Transport Ratio and Predictors Used in the Stepwise Linear Regression. Shown are the Minimum, Median, and Maximum Values for the 36 Models

	Min	Median	Max
Transport ratio, TR	0.09	0.37	0.80
Tortuosity, τ	1.05	1.16	1.51
Standard deviation of the tortuosity, σ_τ	0.009	0.030	0.086
Mean pore size, PS	3.1	3.8	5.2
Standard deviation of the pore size, σ_{PS}	0.60	0.70	1.29
Mean MIP-pore size, MIP-PS	1.1	2.0	3.5
Standard deviation of the MIP-pore size, $\sigma_{MIP\ -\ PS}$	0.31	0.46	0.76
Constrictivity, β	0.14	0.34	0.53
Pore volume fraction, ϵ	0.25	0.35	0.5
Fraction connected pores, ϵ_C	0.980	0.999	1.000

large part of the variation in the data (R^2 = 0.67). There was a clear correlation between the transport ratio and τ but only a very weak correlation with τ_{inlet} (Figure 8).

Discussion

Overall, the transport ratio gave an informative means to compare diffusive transport for different volume fractions. The same pattern was observed for all volume fractions: more disordered pore geometries with low $\theta_{x,y}$-parameter had lower transport rates than more ordered ones, while the increased transport caused by the longer pores resulting from lowering θ_z outweighed the accompanying increase in disorder. The transport ratios for lower volume fractions were markedly lower than for higher volume fractions, and the normalized flux was qualitatively different for different volume fractions. This could be explained as follows. Lowering the volume fraction removes links between pores and increases the number of dead-ends and hence makes the influence of bottlenecks higher, and result in a greater portion of the pore space that does not contribute to diffusive transport.

Stepwise linear regression resulted in quite accurate prediction formulas, both from logarithmic regression and from direct fitting of multiplicative prediction formulas. The ordering of the models given by stepwise fitting was the same for the two methods, and the fitted models were very similar.

As far as we know, standard deviations have not been used before as predictors in the present context. The standard deviations of the tortuosity and of the pore size proved to be

Table 2. Stepwise Linear Regression on the Logarithm of TR, with Some of the Predictors Excluded. The Corresponding Multiplicative Models are Also Shown. $\sqrt{MSE_{log}}$ and R^2_{log} are the Root Mean Squared Error and R^2 Value of the Fitted Regression on the Logarithm, Respectively, $\sqrt{MSE_{mult}}$ are the Corresponding Quantities for Multiplicative Model, and $\sqrt{MSE_{mult,dir}}$ for Multiplicative Model Fitted Directly

Predictors	Fitted Mult. Regression Model	$\sqrt{MSE_{log}}$	R^2_{log}	$\sqrt{MSE_{mult}}$	$\sqrt{MSE_{mult,dir}}$
ϵ excluded	$TR \sim \frac{0.33}{\tau^{4.8}\sigma_\tau^{0.2}}$	0.059	0.991	0.024	0.021
σ_τ excluded	$TR \sim \frac{0.10\epsilon_C^{4.4}PS^{1.4}}{\tau^{5.1}\sigma_{PS}^{0.7}}$	0.070	0.987	0.028	0.023
Only τ and β included	$TR \sim \frac{1.26\beta^{0.2}}{\tau^{6.0}}$	0.092	0.977	0.038	0.029
Only τ included	$TR \sim \frac{0.98}{\tau^{6.3}}$	0.099	0.972	0.039	0.029

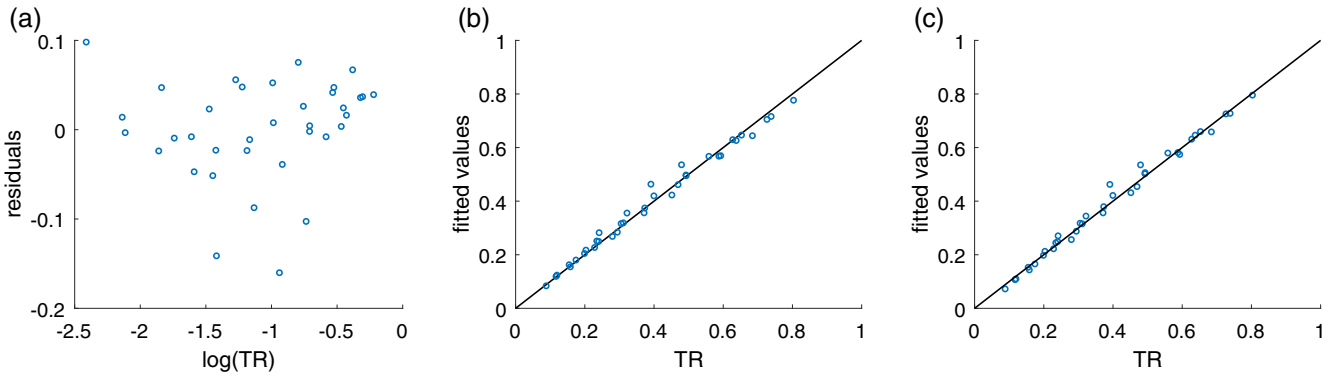

Figure 7. Diagnostic plots for the model $\mathrm{TR} \sim \frac{a}{\tau^b \sigma_\tau^c}$: (a) residuals of the linear regression on the logarithm, (b) the fitted values of the corresponding multiplicative model $\mathrm{TR} \sim \frac{0.33}{\tau^{4.8} \sigma_\tau^{0.23}}$, and (c) the fitted values of the multiplicative model fitted directly, $\mathrm{TR} \sim \frac{0.42}{\tau^{5.5} \sigma_\tau^{0.19}}$.

[Color figure can be viewed at wileyonlinelibrary.com]

Table 3. Linear Regression on the Logarithm of TR, with the Exponent of τ Fixed to the Theoretically Motivated Value. The Corresponding Multiplicative Model is Shown. The Diagnostic Measures are the Same as Those of Table 2

Predictors	Fitted Mult. Regression Model	$\sqrt{\mathrm{MSE}_{\log}}$	$R^2_{\log}$	$\sqrt{\mathrm{MSE}_{\mathrm{mult}}}$	$\sqrt{\mathrm{MSE}_{\mathrm{mult,dir}}}$
τ, σ_τ	$\mathrm{TR} \sim \frac{0.06}{\tau^2 \sigma_\tau^{0.6}}$	0.140	0.883	0.045	0.045
τ, PS, σ_{PS}	$\mathrm{TR} \sim \frac{0.01 \mathrm{PS}^{5.0}}{\tau^2 \sigma_{\mathrm{PS}}^{4.5}}$	0.150	0.869	0.059	0.050
τ, β	$\mathrm{TR} \sim \frac{1.13 \beta^{0.9}}{\tau^2}$	0.317	0.402	0.109	0.101
τ	$\mathrm{TR} \sim \frac{0.48}{\tau^2}$	0.404	–	0.156	0.145

better complements to the tortuosity than the constrictivity measure β (Tables 2 and 3). In particular, if the tortuosity was fixed to the theoretically motivated value $1/\tau^2$ then the models which included standard deviations explained a much larger part of the variation in the data than the model which used β (Table 3).

Higher standard deviations of tortuosity and pore size were correlated with lower transport rates. This is as expected: The standard deviation of the tortuosity is influenced by the proportion of dead ends and by how well the pore structure is connected, and high standard deviations of the pore size is a measure of variations in pore size. Variations in pore size have long been thought to be an important factor influencing the transport rate. However, our results indicate that it is not just the median values of bottlenecks and pore sizes (as measured by the constrictivity measure β) which are important, but more generally how much the sizes of the bottlenecks and pores vary in the pore structure.

The exponent for the tortuosity of the fitted regression models in Table 2 increased as fewer predictors were included in the model. The same pattern is seen for the fitted models in Stenzel et al.[24] This indicates that high exponents for the tortuosity are caused by the model being too simple. Adding further measures that, for example, quantify the connectivity of the pore network might increase the predictive properties of the regression model, and could possibly decrease the tortuosity exponent further.

The new method 9 for calculating the tortuosity which uses the pointwise tortuosities of all points in the pore space and not just the tortuosities at the inlet resulted in a much better prediction capability for pore structures from a single model. Using the pointwise tortuosities of all points means that pore structures where part of the pore network is not well connected to the rest will have a high tortuosity. These parts of the network which, for example, could include many dead ends, in general have low transport rates. The tortuosity factor τ_{inlet} is

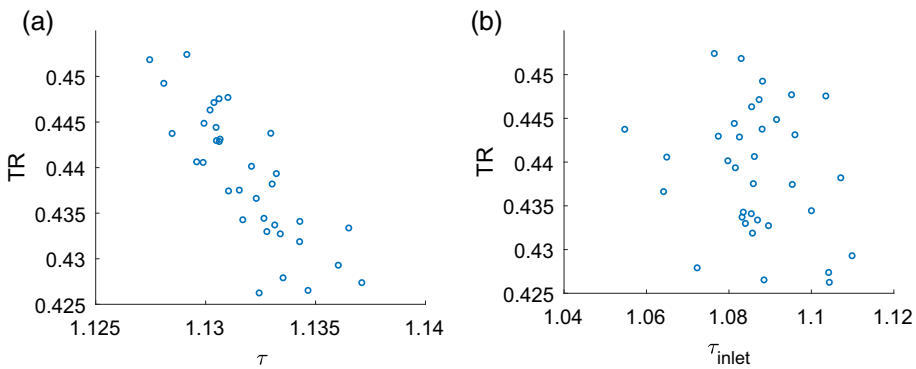

Figure 8. The relationship between transport ratio and (a) τ, (b) τ_{inlet}.

[Color figure can be viewed at wileyonlinelibrary.com]

not sensitive to such parts at all. This might explain why τ has better transport prediction capabilities than τ_{inlet}.

Fitting the model $\text{TR} \sim a/\tau^2$, we obtained $a = 0.48$. The trend is therefore that the transport ratio is around 50% of what it would be if only the tortuosity were limiting the transport rate, as discussed in the section "Average of the reciprocal of the pointwise geodesic tortuosity."

The median values of the pore size and MIP-pore size were used to compute the constrictivity, as described in the section "Constrictivity." For the other measures, we considered the mean of the point-size values for prediction, similarly to how the tortuosity was defined using the mean of the squared inverse point-size values. This is an arbitrary choice, and median values of the pore size and MIP-pore size could also have been considered.

The transport ratio is restricted to lie within the interval [0, 1]. Most of the fitted regression models can take values outside this range, or cannot fill the entire range of possible values. In particularly the models with a value of the intercept $a > 1$, and the models that include standard deviations, can take values larger than 1. As with all regression models, however, it should be expected that they are valid for the range of pore structures and transport ratios they were fitted to, but not for very different structures, such as structures below the percolation threshold, or extremely regular structures.

Effects of Limited Sample Window Size

Theory

The goal is to estimate some measure, for example, the average diffusion or the average or standard deviation of a pointwise geometric measure in an ergodic stochastic pore structure Y_∞ which is unbounded in the x,y-directions, but finite in the z-direction. However, due to computational cost, or the limited size of microscopy images, it is only possible to observe a sample Y of the pore structure in some finite sampling window W. This leads to three kinds of estimation errors.

Stochastic Variation. A measure which is calculated from an observation Y in a finite sampling window will have a random deviation from the measure calculated from Y_∞. Such random errors can be made smaller by using larger sampling windows or by obtaining several samples and, for example, taking averages (or medians) of the measures obtained from the different samples.

Boundary Effects. Numerical calculation of flow in a bounded sample uses boundary conditions at the x,y-boundaries which makes diffusion different in a finite sample than it would have been in an infinite pore structure. Similarly, in calculation of pointwise tortuosity short paths may be cut of by a x,y-boundary. The bias caused by such errors is greater close to these boundaries and can be reduced by computing the values for the entire sample Y, but only using the values in some subwindow $W' \subseteq W$ to estimate of the measure of interest. Here W' has the same thickness as W but voxels in W which are close to the x,y-boundaries are excluded from W'.

Limited Thickness. Measures which are computed for infinite pore structures which are thinner in the z-direction than the structure of interest may differ from the measure of interest. One may be able to get an impression of the size of this bias by computing the measure for structures of different thicknesses, after correcting for boundary effects.

Using only the values in a subwindow to reduce the bias caused by boundary effects makes sample sizes smaller and increases the random error. This is the standard bias-variance tradeoff. Let ψ be the measure of interest. Further let $\hat{\psi}_Y(W')$ be the corresponding measure computed from observations in a finite subwindow W' of the sample window W. Here the subscript Y indicates that the pointwise measures are computed using the entire sample Y. The mean squared error (MSE) which results from using $\hat{\psi}_Y(W')$ to estimate the measure for an infinite pore structure of the same thickness as the sample can be decomposed into a variance component and a bias component, as

$$\text{MSE}(\hat{\psi}_Y(W')) = \text{Var}(\hat{\psi}_Y(W')) + \text{Bias}(\hat{\psi}_Y(W'))^2. \quad (10)$$

Minimizing the MSE thus amounts to balancing these two effects. The variance and bias components may be estimated using several pore structures $Y_1, \ldots, Y_N$, with the bias $E[\hat{\psi}_Y(W') - \psi]$ estimated as $\sum_{i=1}^N \hat{\psi}_{Y_i}(W')/N - \sum_{i=1}^N \hat{\psi}_{Y_i}(W'_0)/N$ using a small subwindow W'_0 which is believed to be relatively unaffected by the boundary effects. Using Eq. 10 this gives an estimate of the MSE, and doing this for several different subwindows W' one can find a subwindow W'_{opt} which minimizes this error. This window size can then be used for estimation of ψ from new samples of this or similar pore structures. In particular, in the next section the subwindow size $226 \times 226 \times 250$ which was used in the section on prediction above is obtained in this way.

Finally, it should be remembered that this optimization only captures boundary effects in the x,y-plane, and ignores bias that might be caused by the sample being thinner in the z-direction than the pore structure of interest.

Results

The results of this section are based on the second simulation experiment which used the model $\epsilon = 0.3$, a high $\theta_{x,y}$ and low θ_z,

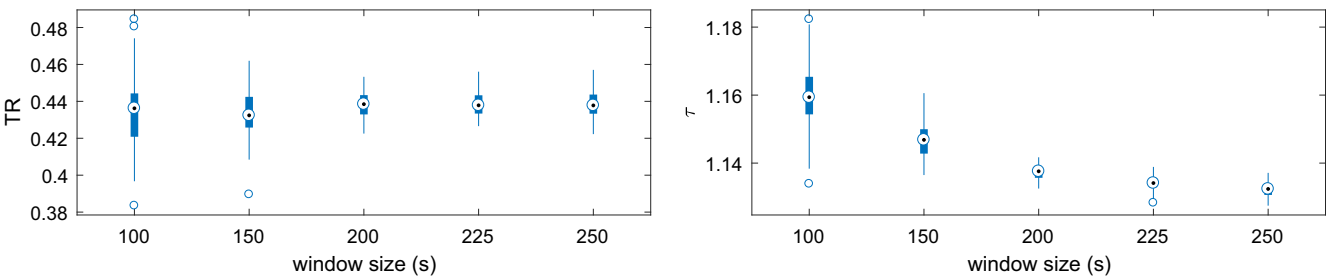

Figure 9. Effect of all three sources of error. Box plots of estimated values of (a) TR and (b) τ, for different sizes $s \times s \times s$ of the sample window W.

[Color figure can be viewed at wileyonlinelibrary.com]

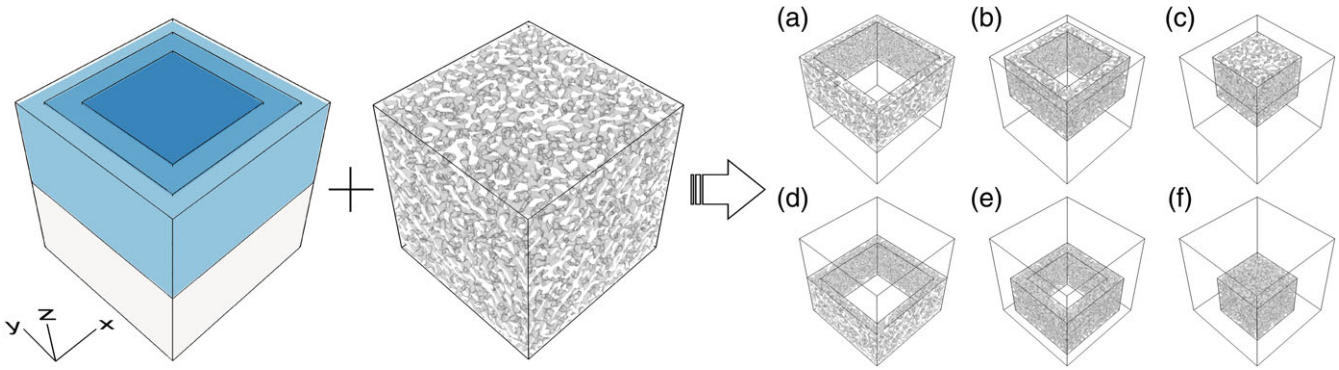

Figure 10. Division of the sample window *W* into six subframes, with three levels in the *x*,*y*-plane and two levels in the *z*-direction.

The resulting division of the pore structure from Figure 3b is shown. Frames (a) and (d) are closest to the *x*,*y*-boundary, and frames (a)–(c) are closest to the inlet. [Color figure can be viewed at wileyonlinelibrary.com]

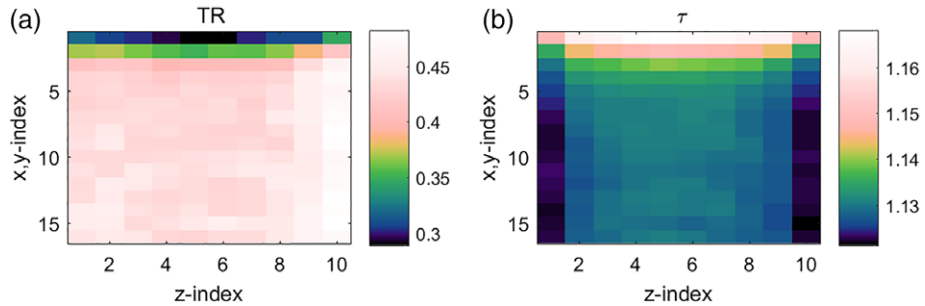

Figure 11. (a) *TR*, and (b) τ, calculated in subframes of the sample window *W*, with 16 levels in the *x*,*y*-plane and 10 levels in the *z*-direction. Each square represents one frame. Frames with *x*,*y*-index one are closest to the *x*,*y*-boundary and frames with *z*-index one are closest to the inlet.

[Color figure can be viewed at wileyonlinelibrary.com]

and simulated 36 pore structures for each window size. Figure 9 shows that, as expected, random variation decreases as the size of the sample window increases. It also illustrates the sum of the bias caused by boundary effects and the bias caused by using thinner sampling windows: the averages of the transport ratios are fairly unaffected by the window size, but instead there is a clear, albeit small, trend in the averages of the tortuosity. Similar results were obtained for the other geometric measures.

To investigate boundary effects we divided the 250 × 250 × 250 sampling window W into subwindows, or "frames" W_F with approximately the same number of voxels, as illustrated in Figure 10. The frames are used to visualize the dependence of the pointwise measures on proximity to the x,y-boundaries and to the inlet and outlet. We computed for each frame the means of the pointwise measures, $\hat{\psi}_Y(W_F)$, for the 36 simulated pore structures, with the pointwise measures computed from the full 250 × 250 × 250 sample window W. Since the transport ratio TR can be expressed as the mean of the normalized flux $J_z/J_{z,opt}$ in the pore space, the pointwise measure corresponding to TR was computed as the normalized flux. The estimated values in frames close to the x,y-boundary differed considerably from the global estimates $\widehat{TR} = 0.44$ and $\hat{\tau} = 1.13$ (Figure 11). The values of τ also deviated from the global estimate in frames close to the inlet and outlet. Additionally, the values of

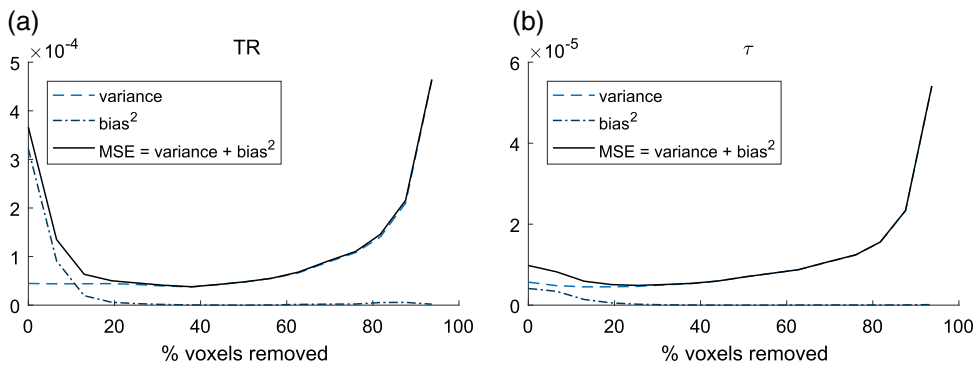

Figure 12. The estimated MSE of the estimator $\hat{\psi}_Y(W')$, where (a) ψ = TR, and (b) $\psi = \tau$, for centered subwindows W' with voxels close to the *x*,*y*-boundary removed. The sizes of the subwindows W' are given as the percentage of voxels removed from the sample window *W*.

[Color figure can be viewed at wileyonlinelibrary.com]

TR deviated from the global estimate in frames close to the outlet.

We used a $166 \times 166 \times 250$ central window W_0' to estimate the bias. It can be seen from Figure 12 that bias caused by boundary effect drops off quickly. Thus, in particular, the choice of the size of the sub-window W_0' did not have a big effect on the estimates of the MSE. The optimal sub-window W_{opt}' seems to be around 80% of the full sample window, taking both *TR* and τ into account. This corresponds to removing 12 voxels at the *x*,*y*-boundaries, i.e. removing frames three steps from the *x*,*y*-boundary (see Figure 11), making the size of W_{opt}' $226 \times 226 \times 250$. The estimated optimal $\sqrt{\text{MSE}}$ were 0.02 and 0.003 for *TR* and τ, respectively, which is 4% and 0.3% of the global estimates. Thus the boundary bias had a bigger impact on the estimation of *TR* than on the estimation of τ.

Discussion

There are clear boundary effects. For pore structures which are similar and of the same size as those in the simulation experiment, removing the 20% of the voxels which are closest to the *x*,*y*-boundaries gives a good compromise between variance and bias. For pore structures which are significantly different it may be advisable to check for the extent of boundary effect as is done in Figure 12.

Figure 11 shows a sizeable difference between calculating the tortuosity factor from the whole sample window vs. from the inlet. The difference between the global transport ratio estimate and values close to the outlet, also visible in Figure 11, is a numerical issue which can be ameliorated by increasing the number of voxels in the numerical diffusion simulations. The resulting transport ratio estimate however was not much affected by increasing the voxel count. Together, these results illustrate the importance of visualizing trends over the sample as is done in Figure 11.

Conclusions

The transport ratio, TR, which is introduced in this article measures the decrease in transport through a film, as compared to a film with an "optimal" pore structure and with the same volume fraction. It hence measures the influence of connectivity, windedness, and thickness fluctuations of the pores and provides a unified way to compare transport in pore structures which have different pore volume fractions. In contrast, related and commonly used measures of "diffusive tortuosity" can not be interpreted in terms of only the windedness of the pores, even though the name suggests this.

Pointwise geodesic tortuosities are defined as the shortest path from the inlet to the outlet going through the point, divided by the thickness of the film. We argue theoretically for computing a tortuosity measure, τ, from the average of one divided by the square of the pointwise geodesic tortuosities over the pore space, and use this as a measure of the windedness of the pores. This is in contrast to standard definitions of geodesic tortuosities which only use the average of lengths of the shortest paths from points on the inlet to the outlet. Further we proposed standard deviations of geometric properties, such as pore sizes and geodesic tortuosities, as additional predictors of transport.

Stepwise regression showed that for the stochastic pore structure model used in this article the average pointwise geodesic tortuosity was the most important geometric predictor of the transport ratio TR (and thus the transport rate). High tortuosity was correlated with low transport rates, and the tortuosity explained a large part of the variation in transport ratios. The constrictivity β, which has been shown to be useful for transport prediction in Stenzel et al.,[24] was not an efficient predictor for this dataset. Instead, higher predictive power was achieved by using standard deviations of tortuosity and pore size, which were inversely correlated with transport ratios. An explanation might be that these standard deviations correlate well with the proportion of pores that do not contribute much to the diffusive transport, either due to bottleneck effects or to dead-end pores. Together, our geometric predictors explained more than 99% of the variation in transport ratios across different model configurations in the simulation experiment. The tortuosity measure we proposed was also shown to be a much better predictor than the standard definition for pore structures from a single model.

A next step will be to apply the stepwise regression to different datasets, either empirical or obtained from different stochastic models, similarly to what was done in Stenzel et al.[24] In that work, the models with β, τ, and ϵ explained a smaller part of the variation in the data than our fitted models (Table 2), likely due to a larger variation between the stochastic models. However, we can take our results as an indicator that our new tortuosity measure τ and the standard deviations provide information that is valuable for diffusive transport predictions.

Clear boundary effects introduced by calculating the geometric predictors and the diffusive transport in finite samples were demonstrated. In the calculations this was corrected for by removing slabs at boundaries and determining the size of the removed slabs by minimizing the mean squared error of transport ratios and of geometric predictors.

Finally, we believe that the insights and methods obtained in this article, and in subsequent research, will inform the design of new and optimized pellet coatings.

Acknowledgments

This work is funded by the Swedish Foundation for Strategic Research (SSF Grant AM13-0066), the Knut and Alice Wallenberg foundation (KAW Grant 20012.0067), and the Swedish Research Council (Grant 2016-04187). We thank Tobias Gebck for help and for the use of the Gesualdo program, Christian von Corswant and everyone involved in the SSF project for valuable discussions, and two anonymous reviewers for very helpful comments.

Literature Cited

1. Heng D, Tang P, Cairney J, Chan H, Cutler D, Salama R, Yun J. Focused-ion-beam milling: a novel approach to probing the interior of particles used for inhalation aerosols. *Pharm Res*. 2007;24(9):1608-1617.
2. James J, Choi HW, Pharoah J. X-ray computed tomography reconstruction and analysis of polymer electrolyte membrane fuel cell porous transport layers. *Int J Hydrogen Energy*. 2012;37(23):18216-18230.
3. Anovitz L, Cole D. Characterization and analysis of porosity and pore structures. *Rev Mineral Geochem*. 2015;80(1):61-164.
4. Mohamad A. *Lattice Boltzmann Method: Fundamentals and Engineering Applications with Computer Codes*. London: Springer; 2011.
5. Chen L, Zhang L, Kang Q, Viswanathan H, Yao J, Tao W. Nanoscale simulation of shale transport properties using the lattice Boltzmann method: permeability and diffusivity. *Sci Rep*. 2015;5:8089.
6. Wang M, Ning P. Predictions of effective physical properties of complex multiphase materials. *Mater Sci Eng R*. 2008;63(1):1-30.
7. Weber A, Borup R, Darling R, Das P, Dursch T, Gu W, Harvey D, Kusoglu A, Litster S, Mench M, Mukundan R, Owejan J, Pharoah J, Secanell M, Zenyuka I. A critical review of modeling transport

phenomena in polymer-electrolyte fuel cells. *J Electrochem Soc*. 2014; 161(2):F1254-F1299.
8. Blunt M, Bijeljic B, Dong H, Gharbi O, Iglauer S, Mostaghimi P, Paluszny A. Pore-scale imaging and modelling. *Adv Water Resour*. 2013;51:197-216.
9. Jones A, Arns C, Hutmacher D, Mithorpe B, Sheppard A, Knackstedt M. The correlation of pore morphology, interconnectivity and physical properties of 3d ceramic scaffolds with bone ingrowth. *Biomaterials*. 2009;30(7):1440-1451.
10. Siepmann J, Siegel R, Rathbone M, eds. *Fundamentals and Applications of Controlled Drug Delivery*. New York: Springer; 2012.
11. Markl D, Strobel A, Schlossnikl R, Bøtker J, Bawuah P, Ridgway C, Rantanen J, Rades T, Gane P, Peiponen KE, Zeitler J. Characterization of pore structures of pharmaceutical tablets: a review. *Int J Pharm*. 2018; 538:188-214.
12. Andersson H, Hjärtstam J, Stadig M, von Corswant C, Larsson A. Effects of molecular weight on permeability and microstructure of mixed ethyl-hydroxypropyl-cellulose films. *Eur J Pharm Sci*. 2013; 48(1):240-248.
13. Marucci M, Arnehed J, Jarke A, Matic H, Nicholas M, Boissier C, von Corswant C. Effect of the manufacturing conditions on the structure and permeability of polymer films intended for coating undergoing phase separation. *Eur J Pharm Biopharm*. 2013;83(2):301-306.
14. Barman S, Bolin D. A statistical model for imaged microstructures of porous polymer films. *J Microsc*. 2018;269(3):247-258.
15. Torquato S. *Random Heterogeneous Materials: Microstructure and Macroscopic Properties. Interdisciplinary Applied Mathematics*. Springer; 2002.
16. Adler P, Jacquin C, Quiblier J. Flow in simulated porous media. *Int J Multiphase Flow*. 1990;16(4):691-712.
17. Roberts A, Teubner M. Transport properties of heterogeneous materials derived from Gaussian random fields: bounds and simulation. *Phys Rev E Stat Nonlin Soft Matter Phys*. 1995;51(5):4141-4154.
18. Mukherjee P, Wang C. Direct numerical simulation modeling of bilayer cathode catalyst layers in polymer electrolyte fuel cells. *J Electrochem Soc*. 2007;154(11):B1121-B1131.
19. Yeong C, Torquato S. Reconstructing random media. *Phys Rev E Stat Nonlin Soft Matter Phys*. 1998;57(1):495-506.
20. Jiao Y, Stillinger F, Torquato S. A superior descriptor of random textures and its predictive capacity. *Proc Natl Acad Sci U S A*. 2009; 106(42):17634-17639.
21. Tahmasebi P, Sahimi M. Reconstruction of three-dimensional porous media using a single thin section. *Phys Rev E*. 2012;85(6):066709.
22. Tahmasebi P, Sahimi M. Reconstruction of nonstationary disordered materials and media: watershed transform and cross-correlation function. *Phys Rev E*. 2015;91(3):032401.
23. Kim S, Pitsch H. Reconstruction and effective transport properties of the catalyst layer in PEM fuel cells. *J Electrochem Soc*. 2009;156(6): B673-B681.
24. Stenzel O, Pecho O, Holzer L, Neumann M, Schmidt V. Predicting effective conductivities based on geometric microstructure characteristics. *AIChE J*. 2016;62:1834-1843.
25. Ghanbarian B, Hunt AG, Ewing RP, Sahimi M. Tortuosity in porous media: a critical review. *Soil Sci Soc Am J*. 2013;77(5):1461-1477.
26. Petersen EE. Diffusion in a pore of varying cross section. *AIChE J*. 1958;5:343-345.
27. Holzer L, Weidenmann D, Münch B, Keller L, Prestat M, Gasser P, Robertson I, Grobéty B. The influence of constrictivity on the effective transport properties of porous layers in electrolysis and fuel cells. *J Mater Sci*. 2013;48(7):2934-2952.
28. Archie GE. The electrical resistivity log as an aid in determining some reservoir characteristics. *Pet Technol*. 1942;1:55-62.
29. Shen L, Chen Z. Critical review of the impact of tortuosity on diffusion. *Chem Eng Sci*. 2007;62(14):3748-3755.
30. Van Brakel J, Heertjes PM. Analysis of diffusion in macroporous media in terms of a porosity, a tortuosity and a constrictivity factor. *Int J Heat Mass Transfer*. 1974;17(9):1093-1103.
31. Carman PC. *Flow of Gases Through Porous Media*. New York: Academic Press; 1956.
32. Epstein N. On tortuosity and the tortuosity factor in flow and diffusion through porous media. *Chem Eng Sci*. 1989;44(3):777-779.
33. Pecho O, Stenzel O, Iwanschitz B, Gasser P, Neumann M, Schmidt V, Prestat M, Hocker T, Flatt R, Holzer L. 3d microstructure effects in Ni-YSZ anodes: prediction of effective transport properties and optimization of redox stability. *Materials*. 2015;8(9):5554-5585.
34. Lindquist W, Lee S, Coker D, Jones K, Spanne P. Medial axis analysis of void structure in three-dimensional tomographic images of porous media. *J Geophys Res Solid Earth*. 1996;101(B4):8297-8310.
35. Thiedmann R, Hartnig C, Manke I, Schmidt V, Lehnert W. Local structural characteristics of pore space in GDLs of PEM fuel cells based on geometric 3d graphs. *J Electrochem Soc*. 2009;156(11): B1339-B1347.
36. Owen JE. The resistivity of a fluid-filled porous body. *J Petrol Technol*. 1952;4(7):169-174.
37. Berg CF. Re-examining Archie's law: conductance description by tortuosity and constriction. *Phys Rev E Stat Nonlin Soft Matter Phys Ther*. 2012;86(4):046314.
38. Camp JJ, Hann CR, Johnson DH, Tarara JE, Robb RA. Three-dimensional reconstruction of aqueous channels in human trabecular meshwork using light microscopy and confocal microscopy. *Scanning*. 1997;19(4):258-263.
39. Moore MJ. Quantitative analysis of interconnectivity of porous biodegradable scaffolds with micro-computed tomography. *J Biomed Mater Res A*. 2004;71(2):258-267.
40. Wiener O. Die Theorie des Mischkörpers für das Feld der stationären Strömung. *Abhandlungen der Mathematisch-Physischen Klasse der Königl Sächsischen Gesellschaft der Wissenschaften*. 1912;32:509-604.
41. Dullien FA. *Porous Media: Fluid Transport and Pore Structure*. New York: Academic Press; 1979.
42. Häbel H, Rajala T, Marucci M, Boissier C, Schladitz K, Redenbach C, Särkkä A. A three-dimensional anisotropic point process characterization for pharmaceutical coatings. *Spat Stat*. 2017;22:306-320.
43. Adler R, Taylor J. *Random Fields and Geometry*. New York: Springer; 2009.
44. Lindgren F, Rue H, Lindström J. An explicit link between Gaussian random fields and Gaussian Markov random fields: the stochastic partial differential equation approach. *J R Stat Soc Ser B Stat Methodol*. 2011;73(4):423-498.
45. MATLAB. Version R2017b. Natick, Massachusetts: The MathWorks Inc., 2017.
46. Münch B, Holzer L. Contradicting geometrical concepts in pore size analysis attained with electron microscopy and mercury intrusion. *J Am Ceram Soc*. 2008;91(12):4059-4067.
47. Gebäck T, Heintz A. A lattice Boltzmann method for the advection-diffusion equation with Neumann boundary conditions. *Commun Comput Phys*. 2014;15(2):487-505.
48. Crank J. *The Mathematics of Diffusion*. Oxford: Oxford University Press; 1979.

Manuscript received May. 11, 2018, and revision received Jul. 13, 2018.